PAPER • **OPEN ACCESS**

Dual-energy CT evaluation of 3D printed materials for radiotherapy applications

To cite this article: Gabriel P Fonseca *et al* 2023 *Phys. Med. Biol.* **68** 035005

IOP Publishing Phys. Med. Biol. 68 (2023) 035005 https://doi.org/10.1088/1361-6560/acaf4a

Physics in Medicine & Biology

IPEM Institute of Physics and Engineering in Medicine

OPEN ACCESS

RECEIVED
1 July 2022

REVISED
20 December 2022

ACCEPTED FOR PUBLICATION
30 December 2022

PUBLISHED
20 January 2023

PAPER

Dual-energy CT evaluation of 3D printed materials for radiotherapy applications

Gabriel P Fonseca[1], **Behzad Rezaeifar**[1], **Niklas Lackner**[1], **Britt Haanen**[1], **Brigitte Reniers**[2] and **Frank Verhaegen**[1]

[1] Department of Radiation Oncology (Maastro), GROW School for Oncology and Reproduction, Maastricht University Medical Centre+, Maastricht, The Netherlands

[2] Research group NuTeC, Centre for Environmental Sciences, Hasselt University, Diepenbeek, Belgium

E-mail: gabriel.paivafonseca@maastro.nl

Keywords: 3D printing, DECT, radiotherapy

Abstract

Objective. There is a continuous increase in 3D printing applications in several fields including medical imaging and radiotherapy. Although there are numerous advantages of using 3D printing for the development of customized phantoms, bolus, quality assurance devices and other clinical applications, material properties are not well known and printer settings can affect considerably the properties (e.g. density, isotropy and homogeneity) of the printed parts. This study aims to evaluate several materials and printer properties to identify a range of tissue-mimicking materials. *Approach*. Dual-energy CT was used to obtain the effective atomic number (Z_{eff}) and relative electron density (RED) for thirty-one different materials including different colours of the same filament from the same manufacturer and the same type of filament from different manufacturers. In addition, a custom bone equivalent filament was developed and evaluated since a high-density filament with a composition similar to bone is not commercially available. Printing settings such as infill density, infill pattern, layer height and nozzle size were also evaluated. *Main results*. Large differences were observed for HU (288), RED (>10%) and Z_{eff} (>50%) for different colours of the same filament due to the colour pigment. Results show a wide HU variation (−714 to 1104), RED (0.277 to 1.480) and Z_{eff} (5.22 to 12.39) between the printed samples with some materials being comparable to commercial tissue-mimicking materials and good substitutes to a range of materials from lung to bone. Printer settings can result in directional dependency and significantly affect the homogeneity of the samples. *Significance*. The use of DECT to extract RED, and Z_{eff} allows for quantitative imaging and dosimetry using 3D printed materials equivalent to certified tissue-mimicking tissues.

1. Introduction

The use of 3D printing technologies allows for rapid prototyping and development of new technologies including several applications in the medical field. This technology brings capabilities to research groups and medical staff that were only available to commercial companies. The radiotherapy field, the focus of this study, has seen the development of novel and centre-specific technologies as custom 3D printed applicators for brachytherapy, QA tools or patient-specific phantoms for imaging and dosimetry. (Fonseca *et al* 2022, Membrive Conejo *et al* 2021, Tino *et al* 2022).

3D printing has been used for dose measurements (Halloran *et al* 2021, Tino *et al* 2022), imaging (Hernandez-Giron *et al* 2019), bolus (Ehler and Sterling 2020, McCallum *et al* 2021), and to accurately position the radiation source in brachytherapy (Liao *et al* 2022, Membrive Conejo *et al* 2021). Therefore, it can affect treatment delivery requiring a thorough evaluation of materials and settings used.

Alssabbagh *et al* compared nine different 3D printing materials against human tissue densities and compositions available in the literature. Alssabbagh *et al* (2017) the study used the mass density provided by the

manufacturer for the raw material before printing, which can differ considerably from the mass density of printed parts depending on the printer settings. Nevertheless, Alssabbagh *et al* is the only study that used spectroscopy to evaluate the elemental composition of the materials encountering traces of calcium, magnesium and metals such as aluminium and titanium which may influence imaging and dosimetry. CT imaging is particularly sensitive to the atomic number due to the predominance of the photoelectric effect for low photon energies. The material composition of 3D printing materials is mostly unknown since commercial filaments can be composed of multiple materials to achieve specific printing properties, colour and mechanical characteristics.

Craft *et al* evaluated four different materials calculating percent depth dose for megavolt photon beams using a treatment planning system compared to measurement. Up to 9 mm differences were observed for the 90% isodose depth if the density of the material is unknown and clinical HU to mass density calibration curves are used instead. Craft *et al* (2018) such a large deviation can occur if the material does not lie on the clinical HU-mass density calibration curve. Significant density variations were observed from samples of the same material indicating possible variation due to printing reproducibility and material homogeneity (Craft *et al* 2018).

Ma *et al* evaluated the largest number of materials (twenty five filaments types for fused deposition modelling (FDM) and 10 resins for polyjet and stereolithography) with CT energies ranging from 70 to 140 kVp resulting in a HU range going from −150 up to 1000 HU when printing solid samples of different materials. HU variations with the photon energy for the printed samples differ from the water (soft-tissue equivalent) behaviour which was attributed to differences in the effective atomic number (Z_{eff}). The interaction of the radiation with the medium depends on the atomic number (Z) which can easily be defined for an atom, but not for a composite media. Z_{eff} is then used to represent the 'atomic number of the media' to evaluate its interaction with radiation. Although Z does not depend on the energy of the photon spectra, Z_{eff} does which can lead to additional uncertainties as extensively described in the literature (Bazalova *et al* 2008, Goodsitt *et al* 2011, Hünemohr *et al* 2014, Saito and Sagara 2017).

This study provides reference values for HU and densities for a range of filaments and could be used to produce radiological phantoms. Z_{eff} for the samples and human tissues were not evaluated. Ma *et al* (2021) multiple studies evaluated 3D printing materials varying the infill to mimic different relative electron densities (RED) or mass densities and represent a wide range of tissue-equivalent materials including lungs (Kairn *et al* 2015, Madamesila *et al* 2016, Mille *et al* 2020a, Park *et al* 2019, Savi *et al* 2020a, 2021, Solc *et al* 2018, van der Walt *et al* 2019). However, the development of bone equivalent materials remains a challenge with studies suggesting the addition of iron (Mille *et al* 2020b) or copper (Savi *et al* 2020a) to achieve HU values equivalent to bone tissue. However, these materials do not have necessarily bone equivalent densities and Z_{eff} is significantly different resulting in different properties than bone for different imaging energies and dosimetry.

This study further evaluates materials used for 3D printing (FDM). A large number of commercial materials and a custom bone filament, including calcium, were evaluated. Dual-energy CT (DECT) (Almeida *et al* 2017, van Elmpt *et al* 2016) was used for the first time to evaluate 3D printing materials extracting Z_{eff} and RED. Although, multiple studies have already evaluated infill (Park *et al* 2019, Savi *et al* 2020a, van der Walt *et al* 2019), other relevant settings such as infill pattern, isotropy, flow, and moisture absorption were evaluated in this study.

The aim of this study is two-fold. Firstly, it will focus on the quantitative evaluation of materials aiming to obtain tissue-equivalent materials based on Z_{eff} and RED ensuring properties will remain equivalent for imaging with different photon energies and also dosimetry in various particle beams used in radiotherapy. Secondly, an extensive evaluation of printing settings, reproducibility and long-term stability will be performed.

2. Material and methods

3D printing materials hereinafter referred to as filaments were selected according to market availability to cover a wide range of filaments including samples of the same material from different manufacturers and different colours of the same material from the same manufacturer.

Standard samples (cylinders or hexagonal prisms) were 3D printed to evaluate material properties and printing settings. The evaluation method described in the following section consists of the evaluation of physical properties and imaging including DECT acquisition to extract Z_{eff} and RED. All samples were printed using either a commercial FDM printer (Model Creality Ender 3, Cordol Technology, Hong Kong) or a custom-made printer (R3D2) designed to work with a wider range of materials.

2.1. Materials

Table 1 shows a list of all the materials evaluated in this study. A total of thirty-one filaments were tested consisting of seventeen material types, ABS and PC filaments from three different manufacturers, and eleven colour variations of an ABS filament from the same brand.

Table 1. List of evaluated filaments. Note that the density refers to the raw filament and not to the printed pieces whose densities will depend on the printing settings such as flow and infill. PC = PolyCarbonate; TPU = Thermoplastic PolyUrethane; PLA = PolyLActide; ABS = Acrylonitrile Butadiene Styrene; ASA = Acrylonitrile-Styrene-Acrylate; PETG = PolyEthylene Terephthalate Glycol; PCTG = Poly—Cyclohexylenedimethylene Terephthalate Glycol; PMMA = polymethylmetacrylate.

Material Type	Brand	Density	Printing temperature °C
PLA			
PLA + Wood (20%)	SunLu	—	170–190
PLA + Cu	HobbyKing	—	205–225
PLA + Al	HobbyKing	—	205–225
PLA + StoneFil Pott. Clay	FormFutura	1.70 g cm^{-3}	190–240
PLA	ESun	1.24 g cm^{-3}	210–230
ABS			
ABS	HobbyKing	—	230–260
ABS	SunLu	—	230–270
ABS (11 colours)	RenkForce	—	220–260
PC and its variations			
PC (polylite)	Polymaker	1.20 g cm^{-3}	250–270
PC	PrimaSelect	1.20 g cm^{-3}	270–290
PC + ABS	Fillamentum	1.07 g cm^{-3}	260–280
PC + PMMA	Verbatin	1.31 g cm^{-3}	220–245
PC	RenkForce	—	—
Other filaments			
PP Transparent	FormFutura	0.90 g cm^{-3}	220–240
PETG	Renkforce	—	230–270
PMMA	Devil design	1.18 g cm^{-3}	225–245
ASA Natural	Fillamentum	1.07 g cm^{-3}	240–255
Bone filament	ColorFab	—	180–220
Nylon PA12	Fiberlogy	1.01 g cm^{-3}	255–270
Nylon CF15 Carbon	Fillamentum	1.08 g cm^{-3}	235–260
PCTG	Fiberlogy	1.23 g cm^{-3}	250–270
TPU	CCTREE	—	230–240

Technical specifications such as chemical composition and density were requested via email to all the manufacturers. The densities (table 1) of some materials are available online or upon request, however, the material composition was not obtained for any of the commercial materials. Often manufacturers replied that filaments are composed of different raw materials from different sources for which the chemical composition was not known to them. Generic information about the composition of these plastics can be obtained, however, colour pigments and other manufacturer-specific additives added to improve finishing, mechanical properties or other material properties are not known. Therefore, it is not possible to estimate how much the composition of each commercial filament differs from generic information available about each type of material.

DECT imaging was used to estimate Z_{eff} and RED overcoming the lack of information about the material composition. A solid cylinder with 2.8 cm diameter and 5.0 cm height was 3D printed for each material using similar settings except for the temperature that had to be adjusted for each material according to the manufacturer's recommendations. All the cylinders were printed using the R3D2 printer with 100% line infill, 0.2 mm layer height and 0.6 mm line width.

The cylinders were placed into a commercial phantom (GAMMEX, Middleton, USA) commonly used for CT calibration as illustrated in figure 1. CT acquisitions were performed for 80, 120 and 140 kVp (Sn filter) using the SOMATON DRIVE CT scanners (SiemensHealthineers, Forchheim, Germany). Images were then processed with syngo.via (SiemensHealthineers, Forchheim, Germany) DECT package that calculates Z_{eff} and RED resulting in three sequences (three tube voltages) and two calculated dataset (Z_{eff} and RED). The dataset was further processed with Matlab (Mathworks, Inc., Natick, MA) to calculate the mean HU, Z_{eff} and RED for each

Figure 1. (a) 3D printed samples used to evaluate the different materials; (b) 3D printed samples inserted in the Gammex phantom (33 cm diameter) during a CT acquisition. Images were reconstructed with an iterative reconstruction kernel Qr40 resulting in a voxel size of 0.732 × 0.732 (pixel spacing) x1 (thickness) mm^3.

insert. A central ROI with 1.5 cm diameter and 1 cm height defined at the centre of each sample was used. Mean and standard deviation (1STD) were calculated including all the voxels within the defined volume.

The density of each insert was calculated by measuring the mass with a 0.01 g precision scale and the volume obtained using a micro-CT with 0.1 mm resolution (XRad 225Cx, Precision x-ray, Inc., North Branford, CT). The micro-CT scan was used to determine the volume of each sample since small variations due to warping and other 3D printing inhomogeneities would not be properly represented by measurements at specific points (e.g. using a ruler or calliper). The higher resolution of the micro-CT compared to a clinical CT provides a more accurate volume estimation and was used only for this purpose. The materials were grouped into four subgroups according to the specific aims.

2.1.1. Control group

Five samples made of transparent ABS (SunLu, Zhuhai, CN) were printed consecutively to evaluate the R3D2 printer reproducibility. ABS is a material susceptible to warping, requires an enclosure and is considered challenging to print. Therefore, the results obtained with this material can be considered representative.

2.1.2. Colours

Eleven samples with different colours of ABS filament from the same brand (RenkForce, Conrad, NL) were printed consecutively to evaluate the effect of the colour pigment in the HU, Z_{eff} and RED.

2.2. Printing settings

Printing settings such as temperature, line width, layer height, infill type and infill density can largely affect the physical properties of the sample. Settings were evaluated for printing hexagonal prisms (figure 2) using 3D printing software Cura (version 4.11, Ultimaker B.V., Geldermalsen, The Netherlands) to process the 3D model and adjust the printing settings. All settings were tested using the same filament (PLA) and printed using the Ender-3 printer (Creality, Hong Kong).

2.2.1. Infill

The infill setting defines the amount of material within a 3D printed sample intercalating regions with filament and air cavities. In addition, to the infill density, the infill type can be chosen from several 2D and 3D options resulting in different geometrical patterns. 2D patterns have been evaluated by other groups (Park *et al* 2019, Savi *et al* 2020a, 2021) and consist of stacked layers with the same geometrical pattern as shown in figure 3(a) where the grey region represents the 3D printer bed indicating that there is no printed material above it when it is visible. Therefore, if a radiation beam hits the sample from above (red arrow in figure 2(b)) it might not interact with any printed material by crossing air cavities whilst lateral radiation beams (blue arrows in figure 2(c)) will always cross a certain amount of material.

3D patterns are composed of stacked layers with varying geometry consisting of stacked pyramids or tilted cubes as shown in figure 3(b). Note that the geometrical arrangement of the printed lines changes with the layers (figure 3(b)—left to right). The 3D printer bed (grey) is not visible indicating that no air channels are present running from top to bottom. Therefore, radiation beams will always cross a certain amount of material

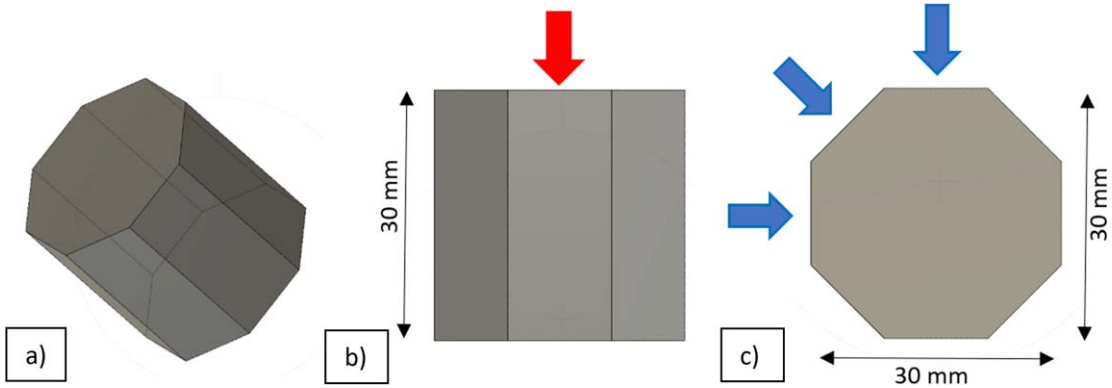

Figure 2. Hexagonal prism with 3 cm distance between opposite faces. (a) 3D model; (b) Orthogonal lateral view. The red arrow indicates the top surface; (c) Orthogonal top view. The blue arrows indicate lateral wall at 0°, 45° and 90°.

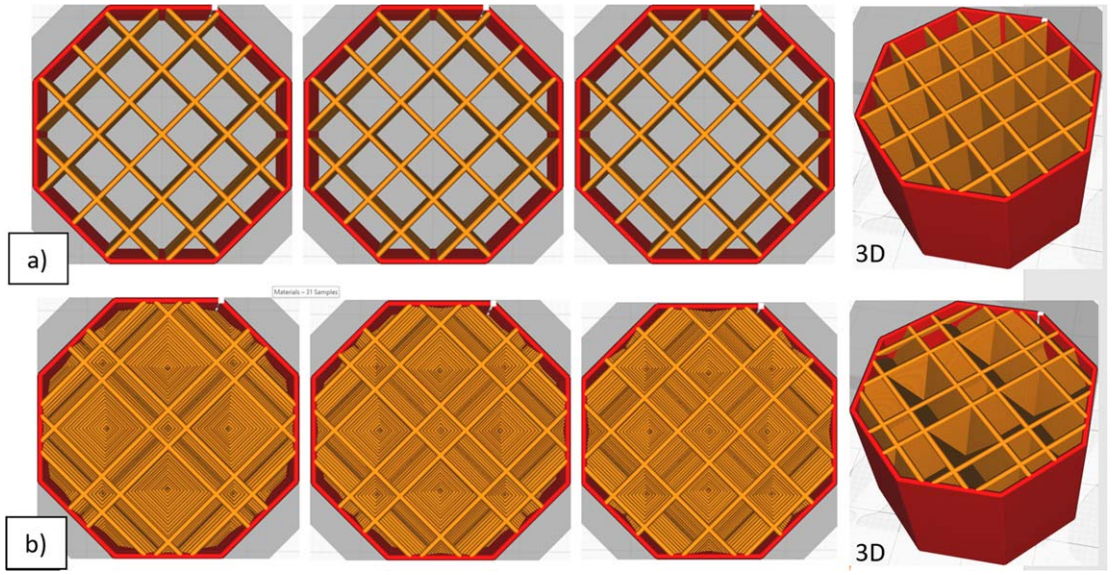

Figure 3. (a) orthogonal top view of consecutive layers of the 3D model using a 2D grid infill and a perspective 3D view. (b) Orthogonal top view of a 3D model using a 3D octet infill consisting of a stack of pyramids and a perspective 3D view. The gray region represents the 3D printer bed.

regardless of the incidence direction. In other words, 3D printed parts are more isotropic or less directional dependent when using 3D infill types since there is no direction from where radiation would cross only air.

Hexagonal prisms were printed with varying infill densities (20, 40, 60, 80, 90, 95 and 100%) for four 3D infill types (cubic, quarter cubic, octet and gyroid) and a 2D grid infill totaling 35 samples. Printed settings were set to 0.1 mm layer height, 0.4 mm wall thickness and 0.4 mm bottom and top thickness. CT acquisitions (120 kV Somaton Confidence) with approximately 0.4 mm voxel width and 1 mm slice thickness were performed by placing the samples into a custom 3D printed phantom as shown in figure 4. The Hounsfield Unit (HU) homogeneity was evaluated by calculating the average HU in a 1.5 cm diameter ROI in a central region with a 1 cm thickness. Isotropy was evaluated by evaluating mass attenuation profiles following the direction represented by red and blue arrows in figures 2(b)–(c).

2.2.2. Printing settings

The physical properties such as density and homogeneity depend on the printer setting as layer height, line width, flow, cooling, retraction and other dozens of settings available on 3D printer software. Most of these aspects were not extensively explored in the literature and can have a relevant effect. For example, the infill density has been studied before but the effect of the line width on the infill has not been evaluated. A thicker line would result in larger gaps than a thinner line for the same infill density. In addition, a thicker line obtained using larger nozzle results in fewer lines, therefore, fewer air interfaces. It is not possible to test all the combinations

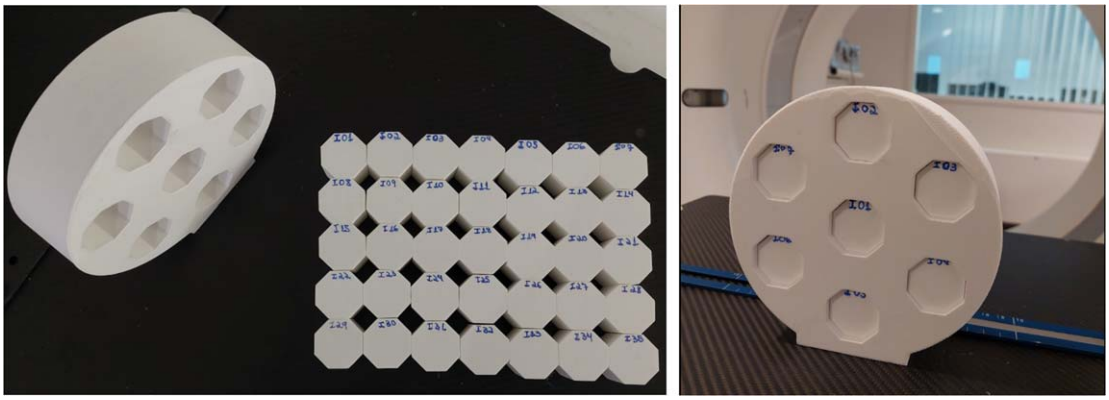

Figure 4. 3D printed phantom and samples used for the evaluation of the infill type. Each infill type was printed with seven different infill densities and scanned in the same acquisition.

due to time constraints so a few settings were tested according to their relevance that was defined based on a few years of extensive experience with 3D printing in our institute.

A total of 36 hexagonal prisms samples were printed using PLA (from the same spool) using an Ender-3 printer. The samples were printed with line widths 0.2, 0.8, 0.9 and 1.0 mm (with a brass nozzle with the diameter equal to the line width), layer height from 0.06 up to 0.4 mm and infill density varying from 40 up to 100%. Usually, more than one setting should be adjusted to obtain optimal results. For example, the flow will increase by using a larger nozzle, therefore, the temperature needs to be increased to allow the extra amount of material to melt or the speed reduced to obtain similar flows. As there is no direct relation between the ideal temperature and flow, the temperature was constant (205 °C) and the printing speed was adjusted aiming to obtain a similar flow regardless of the nozzle size, line width or layer height. Note the flow is direct proportional to the printing time and a larger nozzle diameter would allow for a higher flow (more material can pass through a larger diameter hole in the same time interval). Flow variation can be up to 250 times comparing a sample printed with 0.2 mm (circular area 0.125 mm^2) line width and 0.06 mm layer height (volume = 0.125 * 0.06 = 0.007 54 mm^3) against a sample printed with a 1.0 mm (circular area 3.142 mm^2) line width and 0.6 mm layer height (volume = 3.142 * 0.6 = 1.885 mm^3) per unit of time. It is not possible to have a similar range in the printing speed so we limited the speed range to 5 up to 100 mm s^{-1}.

2.2.3. Tissue equivalence

All the materials evaluated in this study were compared against commercial tissue-mimicking inserts (Gammex) regarding Z_{eff} and RED aiming to identify good tissue substitutes comparable to the well-established Gammex materials used for CT calibration. Reference values for the Gammex inserts were calculated using equations (1) and (2). Where ρ_m is the mass density of the insert, ρ_w the water mass density, w_i is the weight fraction of each element obtained from the chemical composition provided by the manufacturer and z_i/A_i the atomic number per atomic mass obtained from NIST. Although different m values have been described in the literature,(Saito and Sagara 2017, Yang *et al* 2010) this study focuses on the comparison against syngo.via software which is based on the method described by Hünemohr *et al* (2014) that uses $m = 3.1$. This value depends on the photon spectra varying between 2.8 and 3.8 for x-ray energies used for diagnosis (Hünemohr *et al* 2014, Saito and Sagara 2017).

$$\text{RED} = \frac{\rho_m}{\rho_w} \frac{\sum \frac{w_i z_i}{A_i}}{\sum \frac{w_i z_i}{A_i}}, \tag{1}$$

$$Z_{eff}^m = \frac{\sum \frac{w_i z_i}{A_i} Z_i^m}{\sum \frac{w_i z_i}{A_i}}. \tag{2}$$

The calculation was verified by comparing theoretical values against results obtained using DECT acquisitions and syngo.via. CT images (80 and 140 kVp) for seven Gammex inserts (cortical bone, inner bone, CB30, breast, liver, muscle and solid water) following the same process used for the 3D printed inserts. The most promising filaments were selected by comparing Z_{eff} and RED against Gammex tissue-equivalent materials.

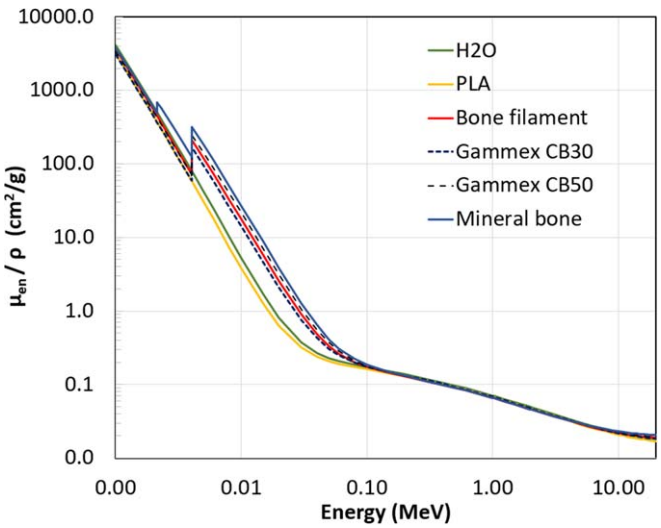

Figure 5. Attenuation coefficients were calculated with XCOM-NIST(Berger *et al* n.d.).

2.2.4. Bone filament

A good substitute for bone tissue has been proven difficult to obtain with some studies recommending the addition of metals (Mille *et al* 2020a, Savi *et al* 2020b). Although, it can result in high HU, similar to bone, the material composition and density are significantly different from bone and not suitable for dosimetry or quantitative imaging performed in radiotherapy.

A custom filament was developed in cooperation with ColorFabb (Belfeld, The Netherlands) aiming to produce a bone-equivalent material regarding composition and density. The production of such a filament is challenging since the addition of calcium makes the material brittle and difficult to print. Therefore, the calcium concentration was limited to 15% (resulting from the addition of 38% $CaCO_3$) added to a compound of PLA and PBAT. The final result has printing characteristics similar to commercial PLA filaments. The exact composition of the bone filament is not known due to the combination of different plastics (raw materials from different manufacturers). Nevertheless, the material does not use colour pigments or any other additive and PLA and PBAT are mostly composed of carbon, oxygen and hydrogen. and were defined as a generic PLA as an approximation. Therefore, our custom bone filament composition was estimated as 62% $C_3H_4O_2$ (PLA) and 38% $CaCO_3$.

Figure 5 shows the calculated total mass attenuation coefficients (Berger *et al* n.d.) of the custom bone filament compared to water, generic PLA, two commercial bone equivalent inserts (Gammex CB30 (30% of $CaCO_3$) and CB50 (50% of $CaCO_3$)) and reference mineral bone(ICRP110 2009).

As the bone filament is not commercially available there was limited information about printing settings and material properties such as mass density and moisture absorption issues. Therefore, eight samples were produced for this material using different settings. Samples were printed before and after drying (2 h at 50 °C) the filament, varying the layer height from 0.1 up to 0.3 mm and increasing filament flow by 5% and 10%.

2.2.5. Long term stability

CT acquisitions were repeated after 150 d using the same CT settings and insert position to evaluate possible material changes due to degradation, absorption of moisture, etc. The Gammex phantom with the 3D printed inserts was scanned with the SOMATOM Drive CT scanner with 80, 120 and 140 kVp.

3. Results

3.1. Control group

The control group samples have similar properties as shown in table 2. Maximum variations of 0.04 g, 0.59 cm^3, 3 HU were observed for mass, volume and HU (all energies) parameters, respectively. RED and Z_{eff} calculated using syngo.via are also consistent between the samples with a maximum variation of 0.002 for RED and 0.08 for Z_{eff}.

Table 2. Control ABS inserts printed consecutively using the same settings and material to evaluate the printer reproducibility. Note that although the settings are the same as used for the colour test, the control inserts were printed using ABS material from Sunlu. Note that the STD of each sample corresponds to the variation within voxels of the same sample whilst the mean STD refers to the variation of the mean value for the different samples.

Label	Mass (g)	Vol. (cm^3)	HU (80 kV)	HU (120 kV)	HU (140 kV)	RED	Z_{eff}
Sample 01	31.82	31.80	-1 ± 24	14 ± 15	36 ± 28	1.051 ± 0.020	6.30 ± 0.55
Sample 02	31.80	31.87	-2 ± 25	14 ± 14	37 ± 27	1.053 ± 0.019	6.22 ± 0.54
Sample 03	31.82	32.03	-1 ± 26	15 ± 15	35 ± 29	1.051 ± 0.020	6.29 ± 0.56
Sample 04	31.84	31.63	-2 ± 25	16 ± 14	36 ± 27	1.053 ± 0.019	6.24 ± 0.56
Sample 05	31.80	31.44	-3 ± 26	14 ± 14	34 ± 29	1.051 ± 0.021	6.23 ± 0.60
Mean ± 1 STD	**31.82 ± 0.02**	**31.75 ± 0.20**	**−1.8 ± 0.7**	**14.6 ± 0.8**	**35.60 ± 1.0**	**1.052 ± 0.001**	**6.26 ± 0.03**

3.2. Colour effect

It is well known among experienced users that the same printing settings might give different results for the same material and the same size if the colour is different since the colour pigment can play a role. Therefore, it was also expected that CT characteristics (HU/Z_{eff}/RED) might differ due to the colour pigment composition. Measured and calculated parameters for the different colours are shown in table 3. Variations are considerably larger than the ones obtained for the control samples (table 2). The largest HU variation was observed between the yellow and brown samples reaching 288 HU (80 kV). The yellow insert has the lowest density (1.062 $g.cm^{-3}$) whilst the brow insert has the second-highest density (1.147 $g.cm^{-3}$). However, inserts with similar density (Orange—1.148 $g.cm^{-3}$ and Brown–1.148 $g.cm^{-3}$) showed relevant HU differences (208 HU—80 kV). The Z_{eff} of the brown sample is 9.46 representing the largest variation from the mean Z_{eff} (6.71).

Figure 6 shows the HU (120 kV acquisition) as a function of the RED and Z_{eff} and also the relation between RED and Z_{eff} for each colour. Z_{eff} is within one standard deviation for all the inserts but the brown sample. Values are mostly within one standard deviation also for RED but it is possible to distinguish three main regions with the yellow sample below 1, grey and purple between 1.00 and 1.05 and the remaining samples between 1.05 and 1.10.

3.3. Infill type

Figure 7 shows CT slices for all the infill types and densities where geometrical variations can be observed in the axial and sagittal directions. The infill patterns are mostly visible in the CT image for low infill and depend on the infill type. Patterns are visible for quarter cubic and octet types up to 90% infill (figure 7(a),(b)) whilst the pattern is barely noticeable for the gyroid type with 40% infill (figure 7(c)).

The 2D grid pattern has air gaps or channels crossing the whole sample which is visible in the sagittal view (figure 7(e)). The red arrow indicates a direction where a radiation beam coming from above would cross mostly an air gap whilst an adjacent beam (green arrow) would cross a solid wall. Note that for all 3D infill types radiation beams coming from any direction would cross both air and plastic since there are no air gaps crossing the whole insert for these patterns. The directional dependence of the infill types will be discussed in the next section.

Table 4 shows the mean HU and standard deviation obtained for different infill types and densities. The standard deviation is inversely proportional to the infill density so a higher infill results in more homogeneous samples. The only exception was observed for the gyroid infill of 100% which showed a larger standard deviation. This infill type requires accurate and fast movements resulting in more vibration and movements than any other infill based on visual inspection during the printing process. We hypothesize that 100% gyroid infill required very small movements to print the wave-like pattern for which the printer precision was not enough resulting in some heterogeneities. The Gyroid infill has the highest homogeneity for infill densities below 60% with similar results obtained with a cubic infill type. Quarter cubic and octet resulted in less homogeneous samples with a worse result than the 2D grid pattern for the majority of the samples.

The relation between infill densities and HU was investigated further for the cubic and gyroid infill types that showed higher homogeneity. Figure 8 shows a strong linear correlation between HU and infill density for both infill types. Therefore, linear regression can be used to define the infill density to obtain the desired HU value.

3.3.1. Isotropy

Figure 9 shows line profiles for the gyroid, cubic and grid 2D patterns obtained with infill densities of 20, 40, 60, 80 and 95%. The lateral profile (figure 2(c)—vertical orientation and figure 7 axial view) represents a line approximately crossing the centre of the insert (solid line) and a line shifted by four voxels (dashed line). The top-to-bottom profile (figure 2(b) and figure 7 sagittal view) corresponds to a line approximately at the centre (solid line) and a line shifted by four voxels (dashed line). Note that the coordinates of the line of the top-to-

Table 3. Results were obtained for 11 different colours of ABS from Renkforce. Materials were printed using the same settings and consecutively in the same printer. The control group was printed right after to ensure observed differences are due to the colour pigment.

Colour	Mass (g)	Vol (cm^3)	Density ($g.cm^{-3}$)	HU 80 kV	HU 120 kV	HU 140 kV	RED	Z_{eff}
Orange	32.76	28.54	1.148	29 ± 25	37 ± 13	68 ± 27	1.085 ± 0.019	6.23 ± 0.54
Blue	31.81	28.27	1.125	20 ± 28	29 ± 15	57 ± 31	1.073 ± 0.023	6.28 ± 0.58
Purple	31.84	28.67	1.111	-1 ± 26	5 ± 14	34 ± 29	1.048 ± 0.021	6.38 ± 0.54
Gray	31.26	28.18	1.101	-22 ± 25	-2 ± 14	10 ± 24	1.024 ± 0.018	6.45 ± 0.51
Red	32.62	29.17	1.118	24 ± 24	30 ± 11	59 ± 25	1.075 ± 0.017	6.35 ± 0.52
White	33.59	28.55	1.177	80 ± 24	63 ± 11	95 ± 25	1.102 ± 0.017	7.03 ± 0.40
Yellow	30.60	28.82	1.062	-51 ± 25	-30 ± 13	-18 ± 26	0.997 ± 0.020	6.34 ± 0.57
Natural	32.49	28.51	1.140	31 ± 23	50 ± 12	63 ± 23	1.078 ± 0.016	6.46 ± 0.46
Brown	33.34	29.06	1.147	237 ± 25	163 ± 14	132 ± 24	1.086 ± 0.017	9.46 ± 0.26
Green	32.77	28.98	1.131	31 ± 24	47 ± 13	63 ± 23	1.077 ± 0.016	6.49 ± 0.47
Black	33.02	29.07	1.136	31 ± 23	48 ± 13	65 ± 23	1.081 ± 0.016	6.39 ± 0.48
Mean ± 1STD	**32.37 ± 0.86**	**28.71 ± 0.32**	**1.127 ± 0.028**	**37 ± 71**	**40 ± 49**	**57 ± 37**	**1.066 ± 0.030**	**6.71 ± 0.90**

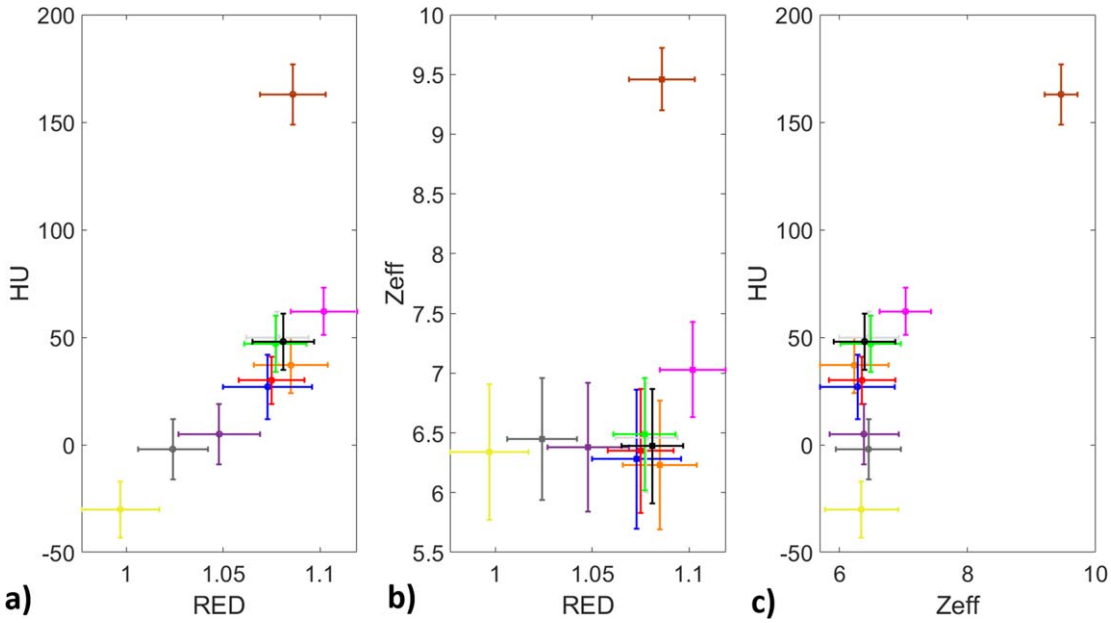

Figure 6. (a) HU as a function of the RED; (b) Z_{eff} as a function of RED; (c) HU as a function of Z_{eff}. The colour of each data point corresponds to the colour of the material used except for the white filament represented as pink to improve visibility and the natural filament represented as light grey.

bottom profile were defined to cross a wall (solid line) and an adjacent air gap (dashed) line for the Grid 2D pattern to show the largest difference.

The HU varies with the position with larger differences for low infill densities (e.g. 20 and 40%). The gyroid infill is more homogeneous with HU profiles resembling a straight line for infill densities above 20% whilst large oscillations are still observed for cubic (infill density up to 60%) and grid 2D (infill density up to 40%). Note that the grid 2D pattern is more homogenous than the cubic pattern considering HU variation in the same line profile. However, significant differences were observed comparing lines profile in the same direction shifted by four voxels (solid and dashed lines) for the grid 2D pattern. The mean values of the reference and shifted profile differed by up to 20, 100 and 33 HU in the lateral direction for the gyroid, cubic and grid 2D patterns, respectively. The maximum differences for the top-to-bottom profiles are 29, 40, and 427 HU for gyroid, cubic and grid 2D patterns, respectively.

The average HU obtained from lateral lines profiles and top to bottom profiles are shown in table 5. The top to bottom orientation has a greater standard deviation indicating large differences between the 3D printed layers in comparison to the lateral profiles. The top to bottom standard deviation is consistent with the ones for the lateral profiles for infill densities from 40% (gyroid), 80% (cubic) and 60% (grid 2D). Cubic and grid 2D patterns showed angular dependence with a larger standard deviation for lateral direction (90°– Cubic and 45°– Grid 2D) for low infill densities whilst the gyroid infill was homogenous from all lateral directions. Nevertheless, the mean HU was obtained for the four evaluated directions within one standard deviation.

3.4. Settings

The effect of the layer height on HU was first evaluated for solid pieces printed with 100% infill. An increase in layer height from 0.06 to 0.10 mm using a 0.2 mm nozzle resulted in lower HU values (on average 48 HU difference) regardless of the 100, 110 or 120% flow rate. Differences due to the layer height were lower using a 0.6 mm nozzle with less than 21 HU difference using a 0.1 and 0.4 mm layer height and only 4 HU variation comparing a 0.2 mm against 0.4 mm layer height.

The line width resulted in similar homogeneity when using a 0.2 and 0.8 mm line for a 100% infill. However, larger variations were observed for lower infill densities. Figure 10 shows CT slices of samples printed with 0.2 and 0.8 mm line widths and the same infill type (cubic) and flow (120%). Thicker lines require larger air gaps to achieve the same infill patterns as thinner lines which resulted in visible patterns and larger standard deviations. Results obtained with a 40% infill using a 0.2 mm nozzle has an 11 HU standard deviation compared to 317 HU standard deviation obtained with a 0.8 mm line width.

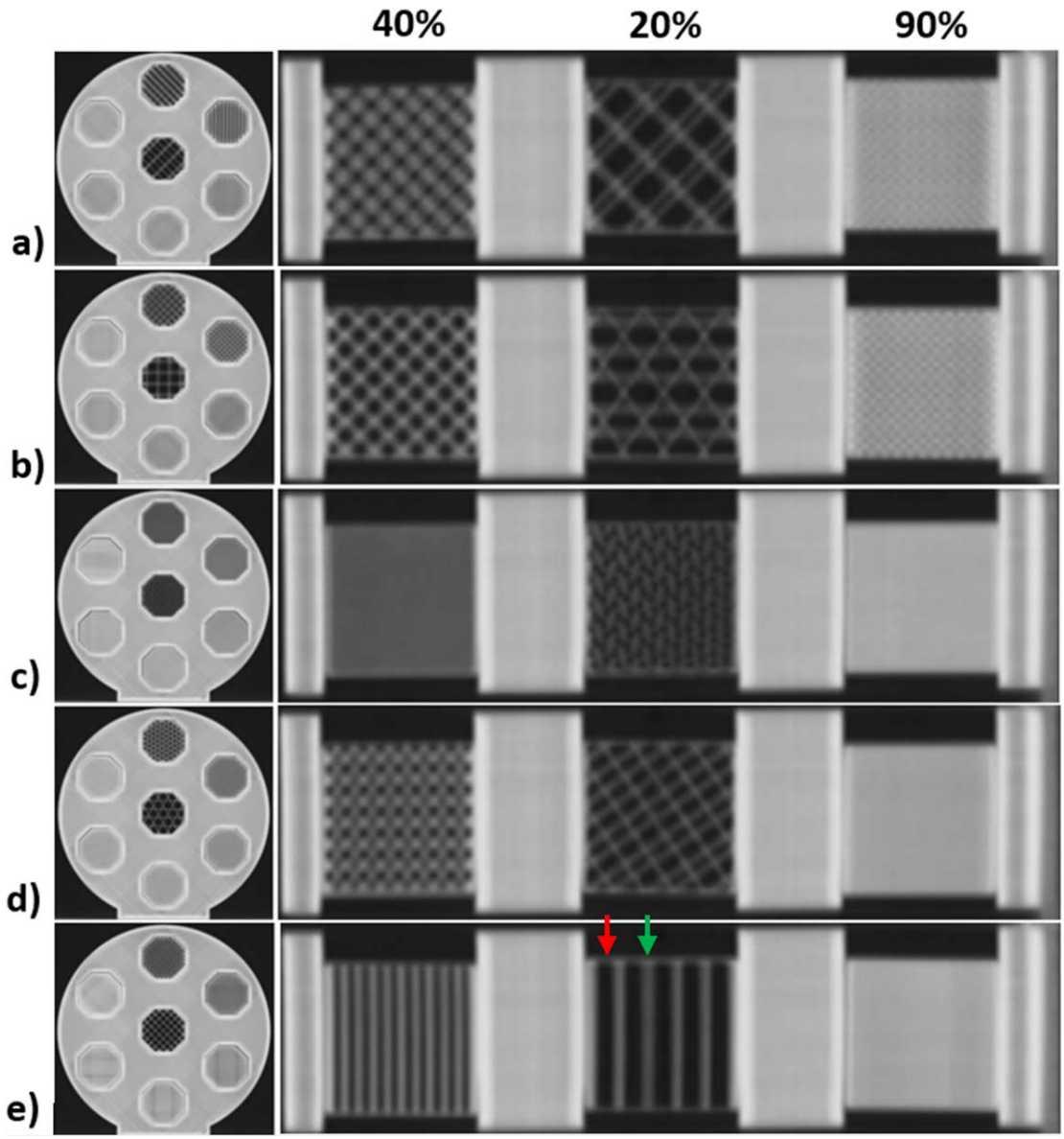

Figure 7. CT acquisition for different infill types and densities. Each row represents one infill type and shows an axial (left) and sagittal (right) view. Infill type from top to bottom quarter cubic (a) octet (b) gyroid (c) cubic (d) grid 2D (e). The central insert (axial view) corresponds to the lowest infill density (20%) followed by the insert on the top (40%) with infill density (60, 80, 90, 95 and 100%) increasing in the clockwise direction. The sagittal view crosses the top, central and bottom inserts corresponding to 40, 20 and 90%, respectively. The red arrow indicates a direction where the radiation beam coming from above would cross mostly an air gap whilst the green arrow indicates a region where radiation would cross a solid wall.

Table 4. HU values ± 1 STD for different infill types and densities. The values were obtained in a 1.5 cm diameter ROI covering 10 consecutive slices.

Infill %	Quarter Cubic	Octet	Gyroid	Cubic	Grid - 2D
20	−858 ± 109	−858 ± 109	−828 ± 58	−845 ± 109	−861 ± 111
40	−695 ± 130	−705 ± 127	−650 ± 10	−670 ± 104	−675 ± 92
60	−530 ± 95	−542 ± 101	−473 ± 9	−499 ± 51	−492 ± 14
80	−364 ± 47	−396 ± 57	−268 ± 14	−321 ± 10	−282 ± 26
90	−262 ± 38	−277 ± 37	−163 ± 11	−222 ± 8	−180 ± 31
95	−231 ± 27	−219 ± 24	−132 ± 11	−185 ± 11	−141 ± 29
100	−180 ± 18	−176 ± 14	−145 ± 28	−141 ± 9	−104 ± 17

3.5. Bone filament

The bone filament is hygroscopic resulting in significant differences between the sample printed before and after drying the filament. It was possible to hear the sound of water vapour bubbles exploding when the filament was

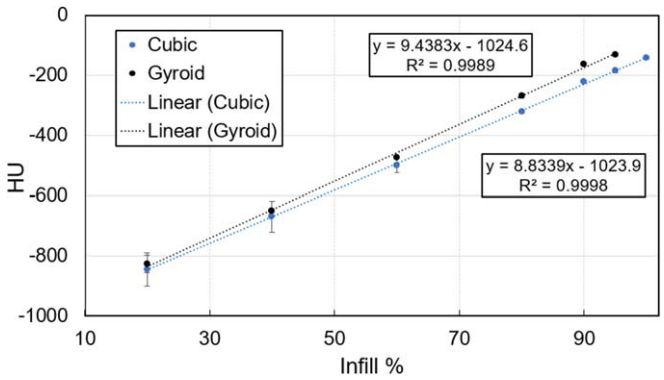

Figure 8. Relation between infill density and HU for two different infill types. The result obtained with the 100% infill for the gyroid infill type was not included since it is not consistent with the remaining values. HU values obtaineted with a 120 kV beam.

being pushed through the nozzle which resulted in an irregular finishing with several gaps in the sample surface. In addition to visual differences, HU increased up to 84 units (80 and 120 kV) whilst the mass and RED increased by approximately 6% after drying the filament.

Results obtained with the bone filament showed larger HU variations due to the printing settings. RED increased from 1.118 to 1.441 after drying the filament and adjusting the printer settings (flow rate increased by 20%). HU also showed a significant increase from 444, 288 and 223 HU to 879, 669 and 581 HU for 80, 120 and 140kV, respectively. On the other hand, Z_{eff} values showed small variations with an average of 11.1 ± 0.1 (1STD) regardless of the RED variation. The Z_{eff} is similar to the commercial Gammex inserts CB30 ($Z_{eff} = 10.6$) and CB50 ($Z_{eff} = 12.6$). Additional, information about the bone inserts is included in the complete material comparison described in the next section.

3.6. Material types

Table 6 shows results obtained for twenty-six evaluated samples including five samples printed with bone equivalent filament with different printing settings. RED varies from 0.712 (PP) up to 1.441 (Bone filament) whilst Z_{eff} goes from 5.22 (PP) up to 12.39 (PLA + Cu) resulting in a wide HU range. Additional samples were printed for the PLA + Stone filament by increasing the flow by 10, 15 and 20% aiming to mimic higherdensity bone tissue. PLA + Al samples were also printed with 30 and 50% cubic infill to mimic lung tissue.

RED and Z_{eff} obtained with syngo.via the Gammex inserts showed maximum differences of 0.02 for RED and 0.14 for Z_{eff} when compared against the theoretical values. The only exception was the adipose tissue insert for which a difference of 0.32 for Z_{eff} was observed.

RED varies significantly with the filament flow rate whilst Z_{eff} showed less variation. PLA + Stone showed a 20% increase in mass density, 23% increase in RED and 3% increase in Z_{eff} when the flow was increased by 20%. The increase was 14% for RED and 1% for Z_{eff} when the flow was increased by 10% and 20% for the same material. Bone filament also showed variations up to 26% for mass density, 29% RED and 3% for Z_{eff} depending on the printing settings.

Table 7 shows the materials with the closest properties to the Gammex inserts. Note that RED can be increased (up to 10%–20%) and decreased for the same material by adjusting the flow and infill whilst Z_{eff} has a much smaller adjustment range. Syngo.via does not calculate Z_{eff} for low-density inserts so Z_{eff} calculated with a solid sample was used as a reference for the low infill samples.

The maximum HU difference was 12 for all the inserts except for bone (80 kV image only) for which up to 25 HU variation was observed. RED variations were below 0.01 for all inserts whilst Z_{eff} variations were less than 0.17 for most of the inserts with a few exceptions. PLA + Stone and Bone filament had up to 0.44 Z_{eff} variation. The largest Z_{eff}, 0.63, difference was observed for the PP filament.

4. Discussion

The use of 3D printing in radiotherapy has been increasing over the years but caution is required when using these materials for quantitative imaging and dosimetry (Kunert *et al* 2022, Ma *et al* 2021). There is a large variety of filaments available in the market with a variety of raw materials that can be combined and also include metal, wood, stone and other additives. There are also different colours for the same type of material so it is an ever-growing list with almost infinite possibilities. Unfortunately, chemical compositions are not known or at least

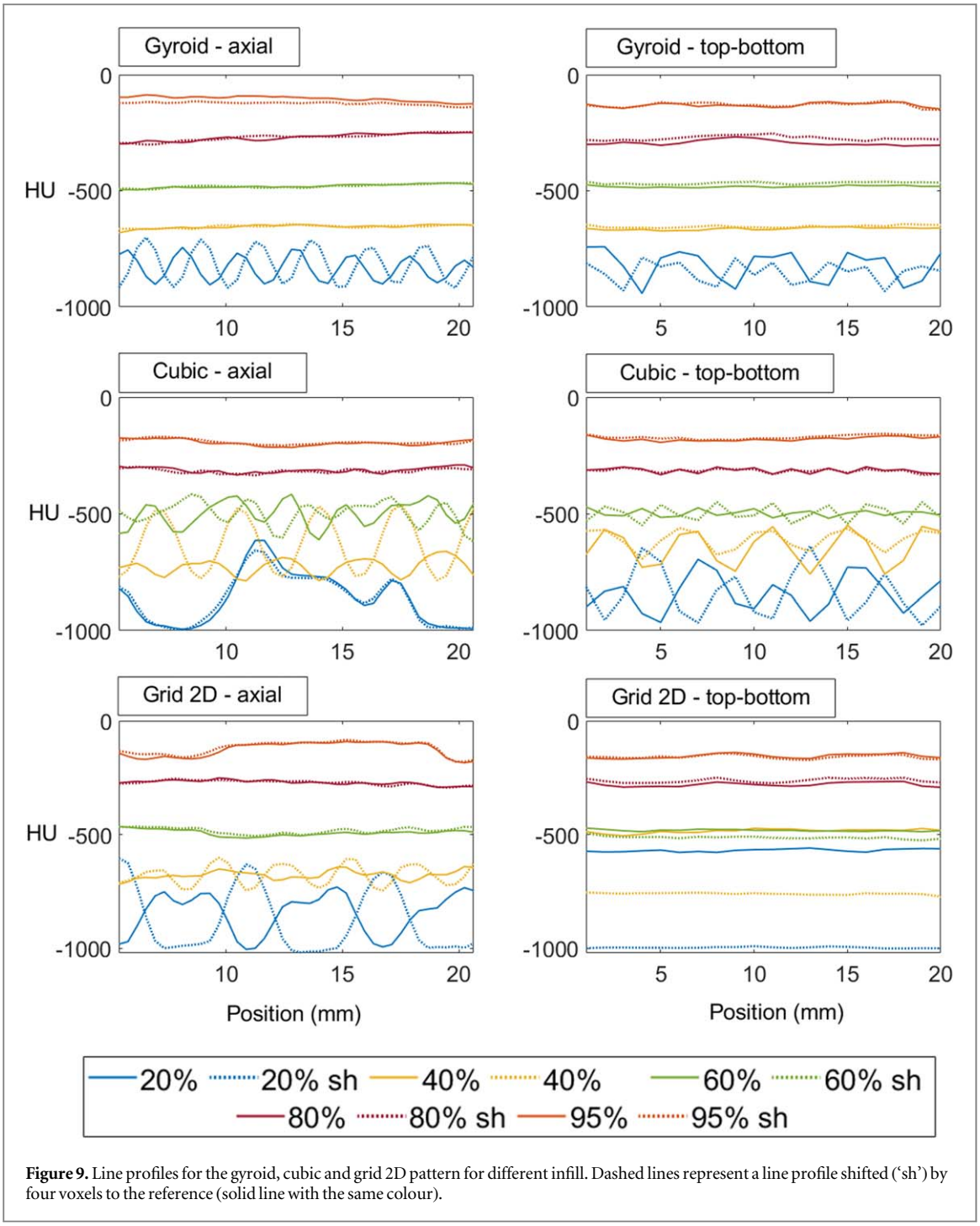

Figure 9. Line profiles for the gyroid, cubic and grid 2D pattern for different infill. Dashed lines represent a line profile shifted ('sh') by four voxels to the reference (solid line with the same colour).

not publicly available so it is not possible to predict the effects of these materials in imaging and dosimetry requiring parts to be printed and evaluated experimentally.

Multiple studies tested 3D printing materials for imaging and dosimetry but the properties of the materials have not been extensively evaluated regarding physical properties relevant for dosimetry and dose calculation in radiotherapy. Materials with metal (e.g. PLA + Cu) (Savi *et al* 2020a) were recommended to mimic bone, which can be a reasonable approximation if one is looking only at HU values for one energy. However, these materials can have low density and only a percentage of high Z_{eff} material resulting in high HU similar to imaging contrast agents. The density of materials with a metal additive does not represent bone so it is not suitable for dosimetry and beam hardening during CT image will also differ from real bone. DECT allows for Z_{eff} and RED measurement so contrast material (e.g. PLA + Cu) will not be mistaken as bone. In addition, the resulting HU depends on the RED, $Z_{eff,}$ tube voltage and filtration so matching 3D printing filaments with tissue-mimicking materials based on HU is not reproducible for different tube voltages which may have different contrast for bony and contrast materials. Kunert *et al* evaluated metal and stone filled filaments for attenuation of x-rays between 70 and 140 kV observing energy dependent deviations from cortical bone for metal filaments whilst stone filled

Table 5. Average HU (±1STD) obtained from lateral lines profiles (figure 2(c)—0°, 45° and 90°) over 20 slices and top to bottom (figure 2(b)) for 20 lines over the same 20 slices.

	Gyroid				Cubic				Grid 2D			
Infill %	Top-Bot.	Lat 0	Lat 45	Lat 90	Top-Bot.	Lat 0	Lat 45	Lat 90	Top-Bot.	Lat 0	Lat 45	Lat 90
20	−804 ± 51	−827 ± 19	−827 ± 14	−822 ± 19	−856 ± 127	−843 ± 18	−844 ± 20	−842 ± 65	−835 ± 100	−859 ± 11	−863 ± 65	−854 ± 10
40	−654 ± 9	−654 ± 6	−652 ± 6	−651 ± 6	−671 ± 108	−668 ± 13	−671 ± 12	−670 ± 58	−671 ± 88	−676 ± 5	−675 ± 62	−677 ± 6
60	−479 ± 8	−476 ± 6	−470 ± 7	−473 ± 7	−498 ± 49	−498 ± 6	−498 ± 6	−497 ± 28	−490 ± 15	−485 ± 7	−488 ± 8	−495 ± 11
80	−283 ± 10	−280 ± 9	−272 ± 11	−276 ± 10	−317 ± 14	−320 ± 8	−320 ± 8	323 ± 8	−270 ± 12	−288 ± 9	−278 ± 15	−281 ± 9
90	−159 ± 11	−162 ± 6	−168 ± 7	−166 ± 4	−218 ± 9	−222 ± 5	−223 ± 7	−222 ± 5	−176 ± 12	−180 ± 10	−173 ± 12	−181 ± 10
95	−130 ± 11	−129 ± 10	−135 ± 7	−135 ± 7	−181 ± 11	−182 ± 8	−185 ± 8	−188 ± 9	−144 ± 25	−133 ± 9	−140 ± 8	−131 ± 11
100	−123 ± 35	−132 ± 8	−142 ± 12	−160 ± 9	−141 ± 11	−142 ± 9	−144 ± 8	−143 ± 7	−103 ± 21	−103 ± 9	−100 ± 11	−101 ± 8

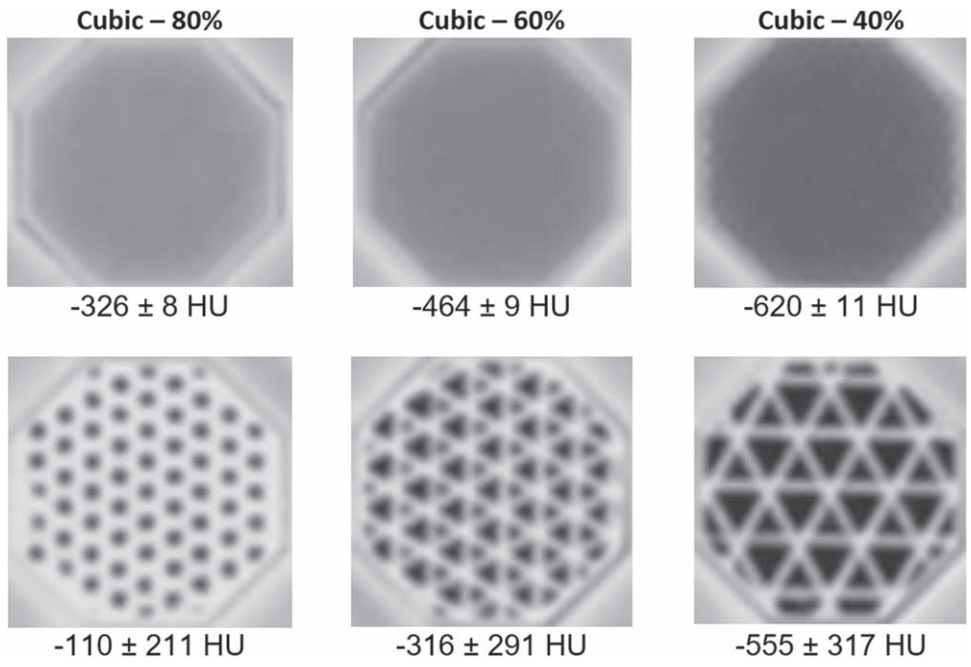

Figure 10. Axial CT slices from samples printed with a 0.2 mm line width (top row) and 0.8 mm line width (bottom row). The average HU and 1STD were obtained in 1.5 cm diameter ROI at the centre of the sample considering 10 consecutive slices. Samples were printed with cubic infill type and infill density of 40, 60 and 80%.

materials deviations were more constant over the evaluated energies (Kunert *et al* 2022). The use of stone filled filaments has also been described by Ma *et al* (2022).

Most publications (Alssabbagh *et al* 2017, Ehler and Sterling 2020) mention the type but not the colour and sometimes the manufacturer of the material. Large differences were observed between manufacturers and for different colours from the same brand due to the colour pigment composition. Users should be aware that colour and brand play a role and this information should be included in future publications to allow a proper comparison between different studies.

Although our control group showed excellent reproducibility, there are many factors including the wearing of mechanical parts and differences due to moisture and spools of the same brand that can affect printing quality and reproducibility. Different manufacturers can have different production tolerances and with exception of our custom bone filament, none of the tested materials was developed for radiotherapy, which can result in additional Z_{eff}, RED and HU uncertainties. The staff and financial costs necessary to evaluate different lots from different manufacturers were prohibitive for this study. Therefore, we implemented a filament QA that requires printing a small sample for each new spool and also after drying the filament, when necessary, so properties can be verified with DECT before using the material to build a phantom. Printing characteristics such as flow and dimension accuracy should also be verified.

The mass of the control samples varied less than 0.04 g (≈0.1%) whilst samples of the same material type from the same brand but with different colours had up to 3 g (≈10%) variations. Such a large variation for samples printed consecutively in the same printer was attributed to the colour pigment that often requires flow and temperature adjustments. Therefore, printing settings should be adjusted for each filament type, brand and colour to obtain the desired finishing, mass and density. We demonstrated that it is possible to vary considerably RED by using variable infill densities and adjusting the flow while Z_{eff} values were less sensitive to these changes allowing only small variations. The mass density and RED showed similar trends when the flow was adjusted due to the increase/reduction of air gaps that affect both parameters. Therefore, mass density can be used as a direct measurement that does not require DECT acquisitions. However, density can be difficult to measure for complex shapes and small volumes for which DECT offers an alternative.

The effect of infill density mimicking different materials has been described (Park *et al* 2019, Savi *et al* 2021) but, to the best of our knowledge, this is the first manuscript to demonstrate the effect of the nozzle size and different infill patterns. A 0.2 mm nozzle size results in highly homogeneous samples with a low infill value (e.g. 40%) that can mimic low-density materials (e.g. lung) whilst a sample with the same infill printed with 0.8 mm is highly heterogeneous with visible infill patterns (figure 10). The higher homogeneity comes at an expense of longer printing times since the larger nozzle represents a 16 times increase in the flow assuming no other

Table 6. Measured properties of the materials evaluated in this study.

ID	Label	Mass (g)	Volume (cm^3)	Density ($g.cm^{-3}$)	HU 80kV	HU 120kV	HU 140kV	RED	Z_{eff}
TRANSPARENT—PC/PCTG/PMMA/PP									
1	PC - Polymaker	32.10	29.40	1.092	−31 ± 29	−16 ± 20	−5 ± 33	1.006 ± 0.025	6.66 ± 0.51
2	PC - PrimaSelect	31.32	30.08	1.041	−67 ± 27	−42 ± 19	−41 ± 33	0.970 ± 0.025	6.54 ± 0.61
3	PC - RenkForce	32.35	30.03	1.077	−49 ± 26	−32 ± 15	−25 ± 25	0.986 ± 0.020	6.67 ± 0.51
4	PC - Verbatin	33.91	29.17	1.162	−0 ± 27	15 ± 15	20 ± 26	1.028 ± 0.020	6.84 ± 0.46
5	PMMA	31.43	28.44	1.105	−2 ± 27	8 ± 15	21 ± 27	1.030 ± 0.020	6.76 ± 0.48
6	PCTG	31.90	29.07	1.097	−27 ± 28	−17 ± 17	−3 ± 27	1.007 ± 0.021	6.71 ± 0.47
7	PP	21.90	28.22	0.776	−327 ± 79	−301 ± 78	−297 ± 104	0.712 ± 0.106	5.22 ± 1.20
8	ABS - RenkForce	29.00	29.16	0.995	−89 ± 27	−69 ± 17	−62 ± 29	0.950 ± 0.022	6.46 ± 0.63
9	ABS - SUNLU	31.82	28.85	1.103	−1 ± 24	14 ± 15	36 ± 28	1.051 ± 0.020	6.30 ± 0.55
ABS - Blue									
10	ABS - RenkForce	31.81	28.27	1.125	20 ± 28	29 ± 15	57 ± 31	1.073 ± 0.023	6.28 ± 0.58
11	ABS - HobbyKing	28.10	28.68	0.980	−117 ± 27	−91 ± 17	−88 ± 32	0.926 ± 0.024	6.34 ± 0.64
PLA - Wood/Stone/Al/Cu									
12	PLA	32.64	28.98	1.126	24 ± 28	18 ± 18	28 ± 31	1.028 ± 0.023	7.35 ± 0.42
13	PLA + Wood	32.71	29.34	1.115	55 ± 27	33 ± 17	33 ± 30	1.022 ± 0.023	8.01 ± 0.35
14	PLA + Stone	38.86	29.63	1.312	702 ± 35	460 ± 24	360 ± 37	1.208 ± 0.027	11.89 ± 0.19
	PLA + Stone+10% flow	43.20	30.45	1.419	824 ± 58	551 ± 51	461 ± 54	1.299 ± 0.048	12.21 ± 0.19
	PLA + Stone+15% flow	46.64	30.38	1.535	1026 ± 34	724 ± 31	618 ± 27	1.438 ± 0.028	12.25 ± 0.16
	PLA + Stone+20% flow	48.17	30.52	1.578	1104 ± 31	789 ± 26	676 ± 33	1.484 ± 0.026	12.30 ± 0.15
15	PLA + Al	31.70	29.50	1.074	−8 ± 28	−21 ± 18	−14 ± 28	0.983 ± 0.022	7.62 ± 0.39
	PLA + Al Cubic infill 30%	12.02	30.52	0.394	−718 ± 23	−687 ± 24	−726 ± 30	0.277 ± 0.023	[a]
	PLA + Al Cubic infill 50%	15.39	30.55	0.503	−526 ± 22	−497 ± 15	−534 ± 22	0.469 ± 0.017	[a]
16	PLA + Cu	34.62	29.68	1.166	608/33	359 ± 21	247 ± 35	1.086 ± 0.025	12.39 ± 0.20
(PC + ABS) / ASA/PETG/TPU/Nylon									
17	PC/ABS	29.13	27.92	1.043	−152 ± 26	−127 ± 16	−122 ± 28	0.891 ± 0.020	6.34 ± 0.35
18	ASA	26.77	28.05	0.954	−202 ± 26	−184 ± 13	−178 ± 26	0.834 ± 0.020	6.44 ± 0.63
19	PETG	33.24	29.52	1.126	−54 ± 26	−49 ± 19	−35 ± 28	0.974 ± 0.022	6.80 ± 0.49
20	TPU	31.36	29.36	1.068	−59 ± 29	−47 ± 21	−31 ± 34	0.981 ± 0.026	6.50 ± 0.58
21	Nylon - Fiberlogy	29.94	29.47	1.016	−40 ± 22	−19 ± 12	−2 ± 20	1.014 ± 0.015	6.08 ± 0.56
22	Nylon - Fillamentum	32.72	29.72	1.100	25 ± 21	43 ± 12	62 ± 19	1.078 ± 0.016	6.19 ± 0.47
Bone									
23	Before drying	36.01	29.35	1,227	437 ± 30	285 ± 24	223 ± 30	1.112 ± 0.022	11.10 ± 0.23
24	After drying	38.28	29.90	1,280	539 ± 30	359 ± 19	293 ± 29	1.184 ± 0.020	11.15 ± 0.23
25	Flow 105%	39.79	29.16	1,365	596 ± 35	396 ± 24	345 ± 32	1.228 ± 0.023	11.15 ± 0.24

Table 6. (Continued.)

ID	Label	Mass (g)	Volume (cm^3)	Density ($g.cm^{-3}$)	HU 80kV	HU 120kV	HU 140kV	RED	Z_{eff}
26	Flow 110%	40.69	28.48	1,429	624 ± 37	448 ± 25	388 ± 36	1.278 ± 0.027	10.88 ± 0.24
27	Flow 120%	45.91	29.77	1,542	882 ± 30	662 ± 20	581 ± 29	1.439 ± 0.020	11.22 ± 0.19

[a] Note that syngo.via does not calculate Z_{eff} for low-density inserts.

Table 7. 3D printed samples compared to GAMMEX tissue-mimicking inserts. Note that RED was included for comparison but these values can still be further adjusted by changing printing settings.

Gammex			Filament		
Material	Z_{eff}	RED	Material	Z_{eff}	RED
Lung In.	7.52	0.280	PLA + Al 30%	7.62	0.277
			PLA Blue	7.35	[a]
Lung Ex.	7.53	0.435	PLA + Al 50%	7.62	0.469
			PLA Blue	7.35	[a]
Muscle	7.49	1.025	PLA + Al	7.62	0.983
			PLA Blue	7.35	1.028
Liver	7.49	1.064	PLA + Al	7.62	0.983
			PLA Blue	7.35	1.086
Breast	6.75	0.962	PETG	6.80	0.974
			PC (various)	6.66–6.84	1.006–1.028
			PMMA	6.76	1.030
Adipose	6.12	0.937	ABS—orange,	6.23	1.085
			ABS—Blue	6.28	1.073
			Nylon - Fiberlogy	6.08	1.014
Brain	6.12	1.038	ABS—orange	6.23	1.085
			ABS—Blue	6.28	1.073
			Nylon - Fillamentum	6.19	1.078
Inner bone	9.97	1.096	ABS—brown	9.46	1.086
CB30	10.62	1.267	Bone—flow 110%	10.88	1.278
CB50	12.24	1.463	PLA + Stone—flow 120%	12.30	1.484
Iodine 10 mg mL^{-1}	11.83	1.006	PLA + Cu	12.39	1.086

[a] Low infill samples were not produced for the PLA-Blue but lower infill and RED can be obtained to mimic lung densities.

parameters have been adjusted. Thicker layers are usually used with larger nozzles so the actual difference in the printing time can be much higher.

Further customization is possible, as demonstrated by Mei *et al* who developed a code to adjust printing properties at the voxel level to create a realistic lung texture (Mei *et al* 2022). A similar approach was used by Okkalidis to print a realistic phantom adjusting the filament flow based on the HU value on each voxel of a reference CT scan (Okkalidis 2018).

In this study, the flow was adjusted to obtain different RED and mass densities so insert properties could be fine-tuned to match desired values. Therefore, printer settings can result in different densities (lower or equal to manufacturer specification) due to micro and macroscopic air gaps, which are not related to the actual material properties. Our study and results from the literature (Savi *et al* 2021) often report measured densities lower than manufacturer specifications. However, we aimed to find tissue-equivalent substitutes and not to obtain the nominal density. Ma *et al* obtained densities differing less than 3% from the specification for most of the materials. The authors mentioned that a time-consuming and tedious optimization of the printer parameters for each material with suboptimal parameters can result in undesired low densities (Ma *et al* 2021).

Infill patterns play a major role in inhomogeneity and isotropy. Gyroid (preferable) and cubic 3D patterns are preferable regarding homogeneity and isotropy with gyroid showing higher homogeneity even for 20% infill samples (table 4) with no visible patterns for infills above 40% (figure 7). 2D infill patterns can still produce homogeneous parts for imaging but the air gaps crossing the samples would result in directional dependence when using the parts for dosimetry which is undesirable. A previous study focusing only on the gyroid infill for a single material also indicates the possibility to obtain homogenous HU regardless of the scanning orientation (Tino *et al* 2019).

All materials were stable after 150 d with larger HU and Z_{eff} variations observed for the bone filament and PLA + Stone possibly due to these materials absorbing moisture from the ambient. The 25 HU deviation observed for the 80 kV image corresponds to 3.9% of the measured bone HU which is consistent with 3.3% (11 HU) variation observed for the 140 kV acquisition after the same 150 d period. The only exception is the PP material for which 0.61 Z_{eff} variation was measured. PP is the only sample with visible air gaps for which syngo. via does not calculate Z_{eff}. Therefore, a small variation in the ROI position between the two acquisitions could lead to a different air volume of air inside and affect the average Z_{eff}.

This study evaluates commercial and custom 3D printing materials using quantitative DECT imaging to obtain parameters, Z_{eff} and RED, used for dose calculation in radiotherapy. The accuracy of DECT derived parameters depends on several aspects such as spectral separation, noise levels, calibration methods, etc.

Hünemohr *et al* reported a mean difference below 0.4 and 2.0% for RED and Z_{eff}, respectively, when evaluating tissue mimicking inserts with a 80–140kV DECT source (similar to the one used in this study). A maximum difference of 6% was report for the Z_{eff} of the brain insert (Hünemohr *et al* 2014), which is consistent with results from (Goodsitt *et al* 2011) that reported up to 6% differences for materials with Z_{eff} above 6.4. Dose calculations and dose measurements, out of the scope of this work, are still necessary to evaluate the use of 3D printed materials for accurate dosimetry.

5. Conclusion

3D printed materials can be used to mimic human tissues with HU, RED and Z_{eff} similar to commercial phantoms currently used for CT calibration in radiotherapy. The evaluated materials cover a large HU range going from lung to bone equivalent materials with the custom bone filament developed for this study showing properties similar to the commercial bone mimicking inserts. Nevertheless, the composition and density of the 3D printing filaments are not well known requiring further evaluation for which DECT can play a role as demonstrated in this study. In addition, printer settings are of major importance regarding isotropy (infill pattern), density and RED (infill density), homogeneity (line width/nozzle size) and reproducibility. The large variety of filament types and printer settings can be highly beneficial for customization but requires careful evaluation before the use for quantitative imaging, dosimetry or during the treatment (e.g. bolus).

ORCID iDs

Gabriel P Fonseca https://orcid.org/0000-0002-8087-1193

References

Almeida I P, Schyns L E J R, Öllers M C, van Elmpt W, Parodi K, Landry G and Verhaegen F 2017 Dual-energy CT quantitative imaging: a comparison study between twin-beam and dual-source CT scanners *Med. Phys.* **44** 171–9

Alssabbagh *et al* 2017 Evaluation of nine 3D printing materials as tissue equivalent materials in terms of mass attenuation coefficient and mass density *Int. J. Adv. Appl. Sci.* **4** 168–73

Bazalova M, Carrier J F, Beaulieu L and Verhaegen F 2008 Dual-energy CT-based material extraction for tissue segmentation in Monte Carlo dose calculations *Phys. Med. Biol.* **53** 2439

Berger M J, Hubbell J H, Seltzer S M, Chang J, Coursey J S, Sukumar R, Zucker D S and Olsen K n.d. *XCOM: Photon Cross section Database (version 1.5 − 2010)*. Retrieved March 7, 2022, from https://physics.nist.gov/PhysRefData/Xcom/Text/version.shtml

Craft D F, Kry S F, Balter P, Salehpour M, Woodward W and Howell R M 2018 Material matters: Analysis of density uncertainty in 3D printing and its consequences for radiation oncology *Med. Phys.* **45** 1614–21

Ehler E D and Sterling D A 2020 3D printed copper-plastic composite material for use as a radiotherapy bolus *Phys. Med. : PM : Int. J. Devoted Appl. Phys. Med. Biol. : Official J. Ital. Assoc. Biomed. Phys. (AIFB)* **76** 202–6

van Elmpt W, Landry G, Das M and Verhaegen F 2016 Dual energy CT in radiotherapy: current applications and future outlook *Radiother. Oncol.* **119** 137–44

Fonseca G P, Voncken R, Hermans J and Verhaegen F 2022 Time-resolved QA and brachytherapy applicator commissioning: towards the clinical implementation *Brachytherapy* **21** 128–37

Goodsitt M M, Christodoulou E G and Larson S C 2011 Accuracies of the synthesized monochromatic CT numbers and effective atomic numbers obtained with a rapid kVp switching dual energy CT scanner *Med. Phys.* **38** 2222–32

Halloran A, Newhauser W, Chu C and Donahue W 2021 Personalized 3D-printed anthropomorphic phantoms for dosimetry in charged particle fields *Phys. Med. Biol.* **66** 22NT01

Hernandez-Giron I, den Harder J M, Streekstra G J, Geleijns J and Veldkamp W J H 2019 Development of a 3D printed anthropomorphic lung phantom for image quality assessment in CT *Phys. Med.: Eur. J. Med. Phys.* **57** 47–57

Hünemohr N, Krauss B, Tremmel C, Ackermann B, Jäkel O and Greilich S 2014 Experimental verification of ion stopping power prediction from dual energy CT data in tissue surrogates *Phys. Med. Biol.* **59** 83–96

Hünemohr N, Paganetti H, Greilich S, Jäkel O and Seco J 2014 Tissue decomposition from dual energy CT data for MC based dose calculation in particle therapy *Med. Phys.* **41** 061714

ICRP110 2009 ICRP Publication 110. Realistic reference phantoms: an ICRP/ICRU joint effort. a report of adult reference computational phantoms *Ann. ICRP* **39** 3–5

Kairn T, Crowe S B and Markwell T 2015 Use of 3D Printed Materials as Tissue-Equivalent Phantoms *IFMBE Proceedings* **51** 728–31

Kunert P, Trinkl S, Giussani A, Reichert D and Brix G 2022 Tissue equivalence of 3D printing materials with respect to attenuation and absorption of x-rays used for diagnostic and interventional imaging *Med. Phys.* **49** 7766–78

Liao Y, Tatebe K, Barry P, Wang D and Turian J 2022 A novel use of 3D-printed template in vaginal HDR brachytherapy *Brachytherapy* **21** 238–43

Ma X, Buschmann M, Unger E and Homolka P 2021 Classification of x-ray attenuation properties of additive manufacturing and 3D printing materials using computed tomography from 70 to 140 kVp *Front. Bioeng. Biotechnol.* **9**

Ma X, Figl M, Unger E, Buschmann M and Homolka P 2022 X-ray attenuation of bone, soft and adipose tissue in CT from 70 to 140 kV and comparison with 3D printable additive manufacturing materials *Sci. Rep.* **12** 1–13

Madamesila J, McGeachy P, Villarreal Barajas J E and Khan R 2016 Characterizing 3D printing in the fabrication of variable density phantoms for quality assurance of radiotherapy *Phys. Med.: Eur. J. M. Phys.* **32** 242–7

McCallum S, Maresse S and Fearns P 2021 Evaluating 3D-printed bolus compared to conventional bolus types used in external beam radiation therapy *Current Med. Imaging* **17** 820–31

Mei K, Geagan M, Roshkovan L, Litt H I, Gang G J, Shapira N, Stayman J W and Noël P B 2022 Three-dimensional printing of patient-specific lung phantoms for CT imaging: emulating lung tissue with accurate attenuation profiles and textures *Med. Phys.* **49** 825–35

Membrive Conejo I *et al* 2021 Custom 3D-printed applicators for high dose-rate brachytherapy in skin cancer *Brachytherapy* **20** 1257–64

Mille M M, Griffin K T, Maass-Moreno R and Lee C 2020a Fabrication of a pediatric torso phantom with multiple tissues represented using a dual nozzle thermoplastic 3D printer *J. Appl. Clin. Med. Phys.* **21** 226–36

Mille M M, Griffin K T, Maass-Moreno R and Lee C 2020b Fabrication of a pediatric torso phantom with multiple tissues represented using a dual nozzle thermoplastic 3D printer *J. Appl. Clin. Med. Phys.* **21** 226–36

Okkalidis N 2018 A novel 3D printing method for accurate anatomy replication in patient-specific phantoms *Med. Phys.* **45** 4600–6

Park S-Y, Choi N, Choi B G, Lee D M and Jang N Y 2019 Radiological characteristics of materials used in 3-dimensional printing with various infill densities *Korean Soc. Med. Phys.* **30** 155–9

Saito M and Sagara S 2017 Simplified derivation of stopping power ratio in the human body from dual-energy CT data *Med. Phys.* **44** 4179–87

Savi M, Andrade M A B and Potiens M P A 2020a Commercial filament testing for use in 3D printed phantoms *Radiat. Phys. Chem.* **174** 108906

Savi M, Andrade M A B and Potiens M P A 2020b Commercial filament testing for use in 3D printed phantoms *Radiat. Phys. Chem.* **174** 108906

Savi M, Villani D, Andrade M A B, Rodrigues O and Potiens M P A 2021 Study on attenuation of 3D printing commercial filaments on standard x-ray beams for dosimetry and tissue equivalence *Radiat. Phys. Chem.* **182** 109365

Solc J, Vrba T and Burianova L 2018 Tissue-equivalence of 3D-printed plastics for medical phantoms in radiology *J. Instrum.* **13** P09018

Tino R, Leary M, Yeo A, Brandt M and Kron T 2019 Gyroid structures for 3D-printed heterogeneous radiotherapy phantoms *Phys. Med. Biol.* **64** 21NT05

Tino R B, Yeo A U, Brandt M, Leary M and Kron T 2022 A customizable anthropomorphic phantom for dosimetric verification of 3D-printed lung, tissue, and bone density materials *Med. Phys.* **49** 52–69

van der Walt M, Crabtree T and Albantow C 2019 PLA as a suitable 3D printing thermoplastic for use in external beam radiotherapy *Australas. Phys. Eng. Sci. Med.* **42** 1165–76

Yang M, Virshup G, Clayton J, Zhu X R, Mohan R and Dong L 2010 Theoretical variance analysis of single- and dual-energy computed tomography methods for calculating proton stopping power ratios of biological tissues *Phys. Med. Biol.* **55** 1343–62